Phonons and magnetoelectric interactions in $Ni_3V_2O_8$

2008 J. Phys.: Condens. Matter 20 434214

(http://iopscience.iop.org/0953-8984/20/43/434214)

J. Phys.: Condens. Matter **20** (2008) 434214 (11pp) doi:10.1088/0953-8984/20/43/434214

REVIEW ARTICLE

Phonons and magnetoelectric interactions in $Ni_3V_2O_8$

T Yildirim[1,2], L I Vergara[3], Jorge Íñiguez[4], J L Musfeldt[3], A B Harris[5], N Rogado[6], R J Cava[6], F Yen[7], R P Chaudhury[7] and B Lorenz[7]

[1] NIST Center for Neutron Research, National Institute of Standards and Technology, Gaithersburg, MD 20899, USA
[2] Department of Materials Science and Engineering, University of Pennsylvania, Philadelphia, PA 19104, USA
[3] Department of Chemistry, University of Tennessee, Knoxville, TN 37996, USA
[4] Instituto de Ciencia de Materiales de Barcelona (ICMAB-CSIC), Campus UAB, E-08193 Bellaterra, Spain
[5] Department of Physics and Astronomy, University of Pennsylvania, Philadelphia, PA 19104, USA
[6] Department of Chemistry and Princeton Materials Institute, Princeton University, Princeton, NJ 08544, USA
[7] Department of Physics and TCSUH, University of Houston, Houston, TX 77204, USA

E-mail: taner@nist.gov

Received 13 May 2008, in final form 3 July 2008
Published 9 October 2008
Online at stacks.iop.org/JPhysCM/20/434214

Abstract

We present a detailed study of the zone-center phonons and magnetoelectric interactions in $Ni_3V_2O_8$. Using combined neutron scattering, polarized infrared (IR) measurements and first-principles LDA + U calculations, we successfully assigned all IR-active modes, including eleven B_{2u} phonons which can induce the observed spontaneous electric polarization. We also calculated the Born-effective charges and the IR intensities which are in surprisingly good agreement with the experimental data. Among the eleven B_{2u} phonons, we find that only a few of them can actually induce a significant dipole moment. The exchange interactions up to a cutoff of 6.5 Å are also calculated within the LDA + U approach with different values of U for Ni, V and O atoms. We find that LSDA (i.e. $U = 0$) gives excellent results concerning the optimized atomic positions, bandgap and phonon energies. However, the magnitudes of the exchange constants are too large compared to the experimental Curie–Weiss constant, Θ. Including U for Ni corrects the magnitude of the superexchange constants but opens a too large electronic bandgap. We observe that including correlation at the O site is very important to get simultaneously the correct phonon energies, bandgap and exchange constants. In particular, the nearest and next-nearest exchange constants along the Ni-spine sites result in incommensurate spin ordering with a wavevector that is consistent with the experimental data. Our results also explain how the antiferromagnetic coupling between sublattices in the **b** and **c** directions is consistent with the relatively small observed value of Θ. We also find that, regardless of the values of U used, we always get the same five exchange constants that are significantly larger than the rest. Finally, we discuss how the B_{2u} phonons and the spin structure combine to yield the observed spontaneous polarization. We present a simple phenomenological model which shows how trilinear (and quartic) couplings of one (or two) phonons to two spin operators perturbatively affects the magnon (i.e. electromagnon) and phonon energies.

(Some figures in this article are in colour only in the electronic version)

1. Introduction

Recent studies have identified a family of multiferroics which display a phase transition in which there develops simultaneously long-range incommensurate magnetic and uniform ferroelectric order. Perhaps the most detailed studies have been carried out on the systems $Ni_3V_2O_8$ (NVO) [1–4] and $TbMnO_3$ (TMO) [5, 6]. For a review, see [7]. This phenomenon has been explained [3] on the basis of a phenomenological model which invokes a Landau expansion in terms of the order parameters describing the incommensurate magnetic order and the order parameter describing the uniform spontaneous polarization. Already from this treatment it was clear that a microscopic model would have to involve a trilinear interaction Hamiltonian proportional to the product of two spin variables and one displacement variable. Furthermore, the symmetry requirements of the phenomenological model would naturally be realized by a proper microscopic model. Accordingly, in this paper we compare detailed combined neutron scattering and polarized infrared studies to first-principles calculations of the optical phonons of NVO and thereby identify which of the experimentally observed phonons have the correct symmetry to induce a dipole moment. We also calculated all possible exchange parameters up to a separation of 6.5 Å and find that only a few of them are significantly large. The aim of our study is to determine which of the zone-center phonons are relevant and which superexchange parameters are important to explain both the observed magnetic structure and also the spontaneous polarization in NVO. This paper therefore sets the stage for a separate quantum calculation of the derivatives of the exchange tensor with respect to atomic displacements.

Briefly, this review is organized as follows. In section 2 we give an overview of the crystal and magnetic structure of NVO. In section 3 we discuss the first-principles calculations of the zone-center phonons and identify those phonons which transform like a vector and thus which are candidates to produce a spontaneous polarization. In this section we also present the neutron scattering measurements of the phonon density of states (DOS) and polarized IR data. The calculations are in good agreement with both neutron and IR data. Next in section 4 we present the calculations of the superexchange parameters up to 6.5 Å cutoff. Then in section 5 we make some qualitative remarks about the spin–phonon interactions and how such an interaction affects the observed phonon and magnon energies at the phase transition. Finally, our conclusions are summarized in section 6.

2. Crystal and magnetic structure of NVO

NVO has an orthorhombic structure [8] with space group *Cmca* [9]. It consists of buckled Kagomé layers of edge-sharing NiO_6 octahedra separated by nonmagnetic VO_4 tetrahedra. Table 1 summarizes fractional coordinates of the six crystallographically inequivalent sites (i.e. Wyckoff positions) in the conventional unit cell. Each such set of Wyckoff positions forms a so-called Wyckoff orbit (WO). There are two WOs of the Ni atoms, the first consisting of the two Ni(c) (a) sites (which we call 'cross-tie' sites) and the second consisting of the four Ni(s) (e) sites (which we call 'spine' sites). The four V (f) sites comprise the third WO and the oxygen sites are distributed into three WOs, an (f) WO containing four O(1) atoms, an (f) WO containing four O(2) atoms and a (g) WO containing eight O(3) atoms. The letters a, e, f and g classify the site symmetry according to the convention of [9]. The locations of these sites are specified in the second column of table 1 and some are also shown in figure 1 (left). Note that there are two formula units of NVO per primitive unit cell or four NVOs per conventional ($a \times b \times c$) unit cell. The Ni sites form buckled planes which have the connectivity of a Kagomé lattice and three such adjacent planes are shown in figure 1 (right). There one sees that the Ni(s) sites (which we call spine sites and which are assigned sublattice numbers s_1, s_2, s_3 and s_4) form chains along the a direction. The Ni(c) sites (which we call cross-tie sites and which are assigned sublattice numbers c_1, c_2, etc) occupy inversion symmetric sites with bonds to nearest-neighboring spine sites forming a cross tie.

NVO is a magnetic insulator whose magnetic properties are associated with the spin-1 Ni^{2+} ions. The buckling of the quasi-Kagomé planes gives rise to a high degree of anisotropy and leads to an interesting and very rich magnetic phase diagram which is characterized by at least three magnetic phase transitions [1, 2, 4]. At high temperatures the system is paramagnetic. When T is lowered through the value $T_{PH} \approx 9.1$ K, an incommensurate phase appears (the high-temperature incommensurate or HTI phase) in which the Ni spins on the spine chains are oriented very nearly along the x axis with an amplitude modulation whose wavevector lies along $\hat{i}$. The axes are denoted either **a**, **b** and **c**, or x, y and z and the corresponding unit vectors are denoted $\hat{i}$, $\hat{j}$ and $\hat{k}$. As the temperature is further lowered through the value $T_{HL} \approx 6.3$ K transverse order appears at the same incommensurate wavevector and also order appears on the cross-tie sites. We call this phase the low-temperature incommensurate or LTI phase. Within the experimental uncertainty, these two ordering transitions are continuous. As the temperature is lowered through the value $T_{LC} \approx 4$ K, a discontinuous transition occurs in which a commensurate antiferromagnetic phase appears. In this phase, antiferromagnetism results from the arrangement of spins within the unit cell in such a way that the magnetic unit cell remains identical to the paramagnetic unit cell. The magnetic phase diagram for NVO is extremely anisotropic with applied field [2, 4] and the complete details of the spin ordering transition in NVO are discussed in [4].

From our previous studies, we find that the complex phase diagram of NVO is basically driven by competing nearest-neighbor (NN) and second NN (SNN) isotropic Heisenberg interactions, denoted J_{1a} and J_{2a} within each chain of spine spins. Because the NiO_6 octahedra are edge-sharing, the NN Ni–O–Ni bond angle is close to 90° so the NN and SNN Ni–Ni interactions are similar in strength [10]. A mean field treatment [11, 12] indicates that, for $J_{2a} > |J_{1a}|/4$, the spine Hamiltonian is minimized by a spin amplitude which is modulated with the wavevector $\mathbf{q} = q_1\hat{i}$, which satisfies $\cos(q_1 a/2) = -J_{1a}/(4J_{2a})$. Putting aside the

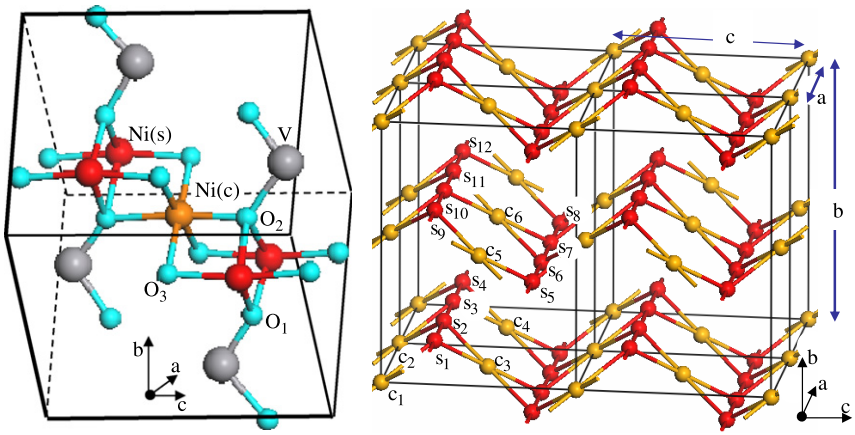

Figure 1. Left: the crystal structure of NVO in its primitive cell. Some of the atoms are not shown for clarity. Right: the buckled Kagomé lattice of Ni sites in NVO. The Ni(s) spine (S) and Ni(c) cross-tie (C) spins are labeled as s_i and c_i, respectively. The buckling is represented by the offset $\delta = 0.13b$ of the spine sites. The cross-tie sites have zero offset and are located at $y = 0$ and $b/2$.

Table 1. The optimized atomic positions using the experimental lattice parameters ($a = 5.922$ Å, $b = 11.372$ Å and $c = 8.225$ Å) in the conventional cell, symmetry decomposition of the Wyckoff sites, and the calculated Löwdin and 3×3 Born-effective charge tensors for the six symmetry independent atoms in NVO. Note that the Born-effective charge tensors have large off-diagonal elements. Also the averages of the diagonal elements of the Born tensors are $-1.9e$, $+4.6e$ and $+2.19e$ for O, V and Ni, respectively. These numbers are very close to the formal charges of these ions and much larger than the calculated Löwdin point charges.

Atoms	Position/decomposition	Löwdin charge	Born eff. charge
(8f)	(0, 0.2487, 0.2327)		−0.763 0.004 −0.005
O(1)	$A_u + 2B_{1u} + 2B_{2u} + B_{3u}$	$-0.62e$	0.000 −3.645 1.424
	$2A_g + B_{1g} + B_{2g} + 2B_{3g}$		0.000 1.575 −1.190
(8f)	(0, 0.001, 0.2453)		−1.008 0.004 −0.009
O(2)	$A_u + 2B_{1u} + 2B_{2u} + B_{3u}$	$-0.68e$	0.000 −3.536 2.135
	$2A_g + B_{1g} + B_{2g} + 2B_{3g}$		0.000 1.955 −2.664
(16g)	(0.2634, 0.1194, 0.0014)		−3.071 −0.371 1.726
O(3)	$3A_u + 3B_{1u} + 3B_{2u} + 3B_{3u}$	$-0.59e$	−0.430 −0.633 0.178
	$3A_g + 3B_{1g} + 3B_{2g} + 3B_{3g}$		1.833 −0.123 −2.089
(8f)	(0, 0.3765, 0.1190)		4.308 0.000 −0.018
V(1)	$A_u + 2B_{1u} + 2B_{2u} + B_{3u}$	$1.18e$	0.000 5.058 0.464
	$2A_g + B_{1g} + B_{2g} + 2B_{3g}$		0.000 0.201 4.371
(4a)	(0, 0, 0)		3.394 −0.005 −0.007
Ni(c)	$A_u + 2B_{1u} + 2B_{2u} + B_{3u}$	$0.9e$	0.000 1.429 −0.633
			0.000 −0.294 2.364
(8e)	(0.25, 0.1310, 0.25)		1.865 −0.001 0.076
Ni(s)	$A_u + 2B_{1u} + B_{2u} + 2B_{3u}$	$0.86e$	0.000 2.567 −0.001
	$A_g + 2B_{1g} + B_{2g} + 2B_{3g}$		−0.689 0.014 2.139

small T dependence of q, we deduce from the experimental value [4] ($q \approx 0.27a*$)[8] in the LTI and HTI phases that $J_{1a} \approx 2.6J_{2a}$. This relation will form a strong constraint on our first-principles calculations of the exchange parameters. Experimentally, it was also determined [1, 4] that the Curie–Weiss constants, Θ_α for a, b and c directions, are 17.0, 19.0 and 20.0 K, respectively. We will use the average $\Theta \approx 18.7$ K as a second experimental constraint on our calculated exchange parameters[9].

Perhaps surprisingly it was found that ferroelectricity observed in NVO coincides with the existence of LTI order, and this behavior was explained by a phenomenological model based on a Landau expansion in powers of order parameters describing ferroelectricity and those needed to describe the magnetic ordering of the HTI and LTI phases [3]. This phenomenological theory elucidates the symmetry of the magnetically induced ferroelectric state. To develop an analogous microscopic theory, one needs to know more about the zone-center phonons in NVO as well as the major superexchange interactions that can couple to the right phonon to induce the observed spontaneous polarization. In the next section, we first discuss the phonons in NVO from combined inelastic neutron scattering (INS), polarized IR measurements and first-principles computations. Next, we determine the important superexchange constants in NVO and discuss how they couple with the zone-center phonons.

[8] To connect this to theory, one must set $q_1 a/2 = (1 - 0.27)\pi$ as explained below equation (17) in [4].

[9] Note that, although Θ is subject to experimental uncertainty, the expression given in equation (73) of [4] is exact (i.e. not subject to fluctuation corrections) for the exchange model.

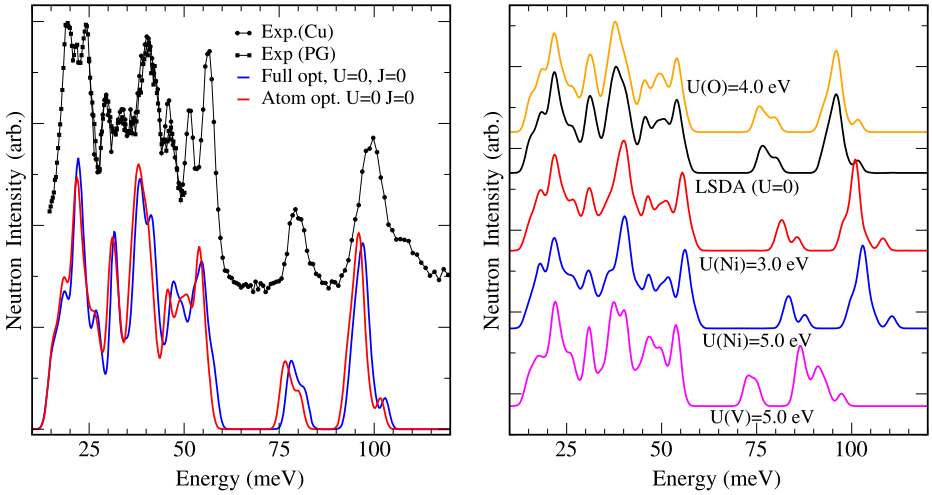

Figure 2. Left: the observed and calculated INS spectra with $U = J = 0$. Note that the calculation with full optimization (i.e. both lattice constant and atomic positions are optimized) agrees with the neutron data very well. Right: the variation of the calculated INS spectrum with different values of U used in LDA + U. The correlation at the oxygen site has almost no effect on the INS spectrum while it corrects the spin-exchange parameters significantly (see the text). The U at the vanadium site affects the calculated INS spectrum very badly, suggesting U(V) should be zero.

3. Zone-center phonons; neutron scattering, polarized IR measurements and first-principles calculations

In this section we present first-principles calculations of the phonons and compare our results with the INS and polarized IR measurements [13–15]. We are able to assign all the observed IR modes and identify the phonons which have the correct symmetry to induce a spontaneous polarization. From calculated Born-effective charges, we also estimate the local distortion which gives rise to the observed dipole moment.

The first-principles total energy and phonon calculations were performed by spin-polarized generalized gradient approximation (GGA) [16] to density functional theory (DFT) [17] as implemented in the code VASP [18]. We used the projector augmented-wave (PAW) method [19] to represent the ionic cores and 400 eV for the plane-wave cutoff energy. Due to well known limitations of LDA in calculations of electronic and magnetic ground-state properties of strongly correlated materials such as transition metal oxides, we used the so-called 'LDA + U' method [20] in our calculations. The LDA + U method presumes that an appropriate set of local orbitals such as 3d can be identified. Then a strong intra-atomic interaction is introduced and treated in a Hartree–Fock manner. The main result is the splitting apart of occupied and unoccupied states within the local orbitals in which the correlations are considered. The strong intra-atomic interactions used in the LDA + U method in a Hartree–Fock manner is characterized by the e–e interaction, U, which can be written in terms of Slater's integrals F^0, F^2, F^4 and F^6 (f-electrons). However, in LDA + U calculations, one does not use the atomic values of the Slater's integrals which would lead to a large overestimate of the true e–e interaction since in solids the Coulomb interaction is usually screened (especially F^0). In practice, these integrals are therefore often treated as parameters, i.e. adjusted until one gets results that are in good agreement with experimental values. They are normally specified in terms of the effective on-site Coulomb and exchange parameters, U and J (i.e. for p-electrons, $U = F^0$, $J = F^2/5$ and for d-electrons $U = F^0$, $J = \frac{1+0.625}{14}F^2$). For transition metal oxides, the typical values are 1–7 eV for U and 0.2–1 eV for J. From extensive studies on cuprates, it was also realized that the oxygen p-orbital correlations could also be very important in addition to d-orbital correlations [21]. Hence, in our study, in addition to Ni d-orbitals, we also consider correlation effects at the oxygen sites and found them to be very important. We vary U as a free parameter to see how it affects the phonon spectrum as well as the superexchange interactions that we discuss in the next section.

In our calculations, we considered the primitive unit cell of the NVO which contains 26 atoms. The lattice parameters and the atomic positions were all optimized to eliminate the forces down to 0.005 eV Å^{-1}. The optimized positions with the experimental lattice parameters are listed in table 1, which are in excellent agreement with the experimental positions (i.e. within 0.01 Å). Using the optimized structure, we next calculated the zone-center phonons from the finite displacement method and the corresponding INS one-phonon spectrum as described in [22].

Figure 2 shows the measured INS spectrum from an NVO powder sample. The INS measurements were performed using the filter analyzer spectrometer (FANS) located on beamline BT4 at the NIST Center for Neutron Research [23]. For energies above 40 meV, a Cu(220) monochromator, surrounded by 60′–40′ horizontal collimation and combined with a cooled polycrystalline beryllium filter analyzer, was used. For the low-energy spectrum (i.e. $E < 40$ meV), a graphite (PG) monochromator with 20′–20′ collimation was used. The relative energy resolution of the FANS instrument is approximately 5% in the energy range probed. The powder

$Ni_3V_2O_8$ sample (about 20 g) was held at 8 K with a helium-filled aluminum can using a closed-cycle He^3 refrigerator.

The measured INS spectrum and the calculations for different values of U are compared in figure 2. The agreement of the calculations to the observed spectrum is quite good, giving further confidence that the first-principles calculations capture the main physics. It also suggests that the phonon modes in NVO have small dispersion with wavevector. This is because the INS spectrum reflects an average over a large range of **Q** but nevertheless agrees well with the calculations which are only for $Q = 0$. The phonon spectrum basically consists of three well-separated energy bands. The first band is between 15–60 meV and is due to rotation/translation (low-energy portion) and small distortion of the NiO_6 octahedra (high-energy portion). The second phonon band is between 75–85 meV. It involves mainly the vibration of the O(2) along the V–O bond. Since all oxygen atoms are also connected to Ni atoms, these modes cannot be described as purely V–O bond stretching because they always have some Ni–O bond stretching as well. Finally, the third phonon band lies in the energy range between 90 and 105 meV. These modes are very similar to the second band, i.e. oxygen vibration along the V–O bond, but they are also mixed with O–Ni–O bending and therefore occur at higher energies.

The right panel in figure 2 summarizes the effect of different values of U on the calculated phonon spectrum. From this figure, it is clear that we do not need non-zero U(Ni) in order to get good agreement with the experimental data. This is also consistent with the measured electronic bandgap of NVO. With $U(\text{Ni}) = 0$, we have a bandgap of about 0.7 eV, which compares nicely with the experimental value of ≈0.5 eV [14]. However, as we will see in the next section, the calculated values of the exchange parameters are very large when $U(\text{Ni}) = 0$. Taking non-zero U(Ni) improves the exchange parameters but then the phonon energies above 80 meV become much larger than the neutron measurement indicates. The U(Ni) also opens a large gap (for example, for $U(\text{Ni}) = 5$ eV, the gap is found to be about 2 eV) which is not consistent with experiment [14]. Accordingly, we also studied the effect of correlations at V and O sites by taking non-zero U(V) and U(O). The bottom phonon spectrum in figure 2 clearly indicates that U(V) softens the VO stretching significantly, yielding very low-energy modes, totally disagreeing with the observed spectrum. Hence, based on this result we conclude that U(V) should be taken as zero. In contrast, the oxygen U is found to have almost no effect on the phonon spectrum. It also does not open the bandgap. However, as we will see in section 4, U(O) improves the magnetic exchange parameters significantly and in particular it is the key parameter to get the right ratio for J_{1a}/J_{2a}.

In order to identify the phonon modes that can induce the observed dipole moment along the **b** axis in NVO, we need to know the symmetry properties of each phonon. The symmetry analysis of the zone-center phonons was carried out in [13]. Below we briefly repeat the symmetry analysis of the phonons and then compare our results with the polarized IR measurements on single-crystal NVO samples.

Table 1 shows the symmetry decomposition for the six Wyckoff sites present in NVO. There are 26 atoms in the primitive unit cell and the representation Γ_u induced by the vector space of these $26 \times 3 = 78$ atomic displacements has the decomposition

$$\Gamma_u = 10A_g + 8A_u + 8B_{1g} + 13B_{1u} + 7B_{2g} + 12B_{2u} + 11B_{3g} + 9B_{3u}. \quad (1)$$

The vector representations which transform like x, y and z are modes of symmetry B_{3u}, B_{2u} and B_{1u}, respectively, and these are the only ones responsible for IR activity. For the observed spin structure, the spontaneous polarization must lie along the b axis [3] and this polarization must result from the condensation of one or more of the twelve B_{2u} symmetry modes [13]. One of the these twelve modes is acoustic (i.e. all atoms move uniformly along the **b** axis) and will not be considered any further.

In addition to mode energies, we also calculated the dipole moment per unit cell $\mathbf{P}_y^{(n)}$ of each mode from the effective Born-charge tensor which is listed in table 1. To estimate the polarization vector of the nth mode, we write the atomic displacement in terms of the eigenvectors $O_{\tau,\alpha}^{(n)}$ as

$$u_{\tau,\alpha} = \sum_n O_{\tau,\alpha}^{(n)} M_\tau^{-1/2} Q_n = \sum_n O_{\tau,\alpha}^{(n)} \sqrt{\frac{\hbar}{2M_\tau \omega_n}} (a_n^\dagger + a_n), \quad (2)$$

where $a_n^\dagger$ is a phonon creation operator. A crude estimate for the polarization vector of the nth mode can then be obtained from the following formula:

$$P_{\text{rms},\alpha}^{(n)} = \frac{1}{\Omega_{\text{uc}}} \sum_{\tau,\beta} Z_{\alpha,\beta}^*(\tau) O_{\tau,\beta}^{(n)} Q_{\text{rms}} M_\tau^{-1/2}, \quad (3)$$

where Ω_{uc} is the volume of the unit cell and $Q_{\text{rms}} = \sqrt{\hbar/2\omega}$ is the average zero-point fluctuation. The $Z_{\alpha,\beta}^*(\tau)$ is the effective Born-charge tensor that we calculated using the Berry-phase method [24]. After having calculated the effective Born charges, it is straightforward to calculate the IR intensities.

Near-normal reflectance of $Ni_3V_2O_8$ single crystals was measured at 300 K over a wide energy range (2.5 meV–6.5 eV) using three different spectrometers as described previously [14, 15]. The infrared reflectance for light polarized along the a, b and c directions is shown in figure 3. The spectral resolution was 0.5 cm^{-1} in the far- and middle-infrared. Polarizers were employed, as appropriate. Data along the a and c directions were collected from the large, shiny natural growth face of a crystal [14, 15]. A cut crystal exposing the b axis was also employed. Here, surface quality issues broaden phonon linewidths and cause slight leakage of a- and c-related features into the spectrum. Despite these challenges, b-polarized phonon positions are highly reliable[10].

Figure 4 displays the optical conductivity, σ_1, extracted from the reflectance measurements shown in figure 3 by a Kramers–Kronig analysis [25]. We also show the calculated intensities from both the Born-effective charges and the simpler Löwdin charges. Not surprisingly, although the agreement

[10] We elected not to polish to avoid additional damage or polishing-induced stress on the crystal.

Table 2. Comparison of calculated (cal.) and experimental (exp.) mode energies (meV) in NVO. The calculated rms dipole moment, $P_{\rm rms}$, is shown in parentheses (in 10^{-4} C m^{-2}). The IR intensity is proportional to $P^2_{\rm rms}$. The relative intensities of the observed modes are also given in parentheses. The abbreviations, vs, s, m, w and vw indicate very strong, strong, medium, weak and very weak, respectively.

	$B_{3u}(a)$		$B_{2u}(b)$		$B_{1u}(c)$	
No.	Cal.	Exp.	Cal.	Exp.	Cal.	Exp
1	18.39 (13.6)	Not obs.	21.32 (9.0)	21.58 (vw)	17.78 (1.0)	Not obs.
2	24.45 (33.7)	25.15 (vw)	24.33 (0.8)	24.90 (w)	22.97 (2.6)	23.27 (vw)
3	30.13 (85.7)	29.77 (m)	27.40 (18.3)	27.83 (w)	26.48 (8.1)	27.12 (vw)
4	38.88 (10.0)	38.34 (vw)	36.06 (76.3)	36.01 (m)	31.37 (69.9)	31.89 (vw)
5	41.85 (35.4)	41.59 (vw)	39.72 (1.3)	40.77 (w)	37.47 (0.7)	37.63 (vw)
6	46.60 (42.7)	45.93 (w)	40.52 (65.4)	40.11 (m)	39.02 (53.3)	40.00 (w)
7	52.68 (29.3)	52.54 (w)	50.24 (19.4)	50.51 (w)	41.05 (3.25)	Not obs.
8	100.22 (161)	97.55 (vs)	55.68 (12.3)	56.16 (w)	46.62 (45.7)	46.31 (w)
9	—	—	83.82 (176)	78.19 (s)	56.44 (3.3)	Not obs.
10	—	—	102.81 (64.5)	100.42 (m)	82.51 (139)	77.95 (s)
11	—	—	110.62 (57.0)	109.3 (m)	101.19 (65.0)	97.55 (m)
12	—	—	—	—	103.34 (100)	102.35 (m)

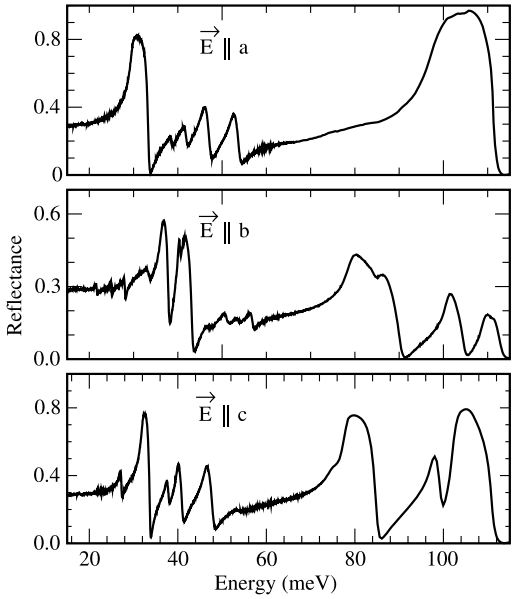

Figure 3. Room temperature reflectance spectra of $Ni_3V_2O_8$ for light polarized along the a, b and c directions.

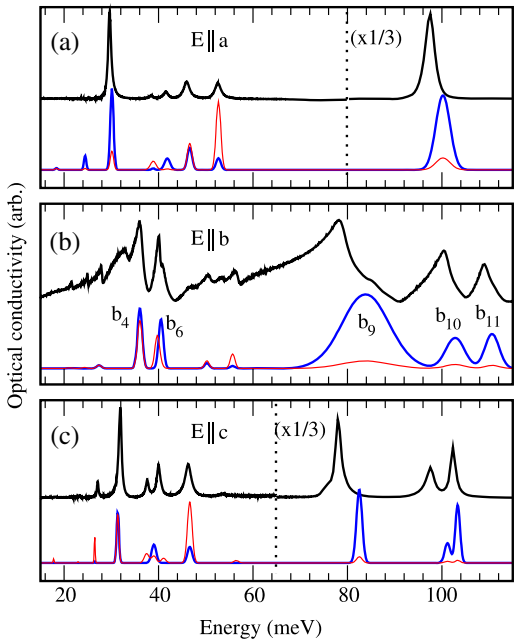

Figure 4. Room temperature optical conductivity of $Ni_3V_2O_8$ (black) for light polarized along the a and c directions (from [14]) and along the b direction (this work), extracted from reflectance measurements by a Kramers–Kronig analysis. For better visualization, in panels (a) and (c) the intensities of high-energy modes (above 65 meV) were reduced by a factor of three. The calculated IR intensities from Born-effective charges (heavy blue line) and Löwdin charges (light red line) are also shown. The modes for $E \parallel \mathbf{b}$ are numbered as in table 2. The calculations were for U(Ni) = 5.0 eV and J(Ni) = 1.0 eV, which overestimate the high-energy modes by about 3–5%. The calculated IR intensities are plotted as Gaussians with widths that roughly match the observed spectrum.

between Löwdin intensities and IR data is poor, we have excellent agreement between the Born intensities and the IR data. The calculated and measured phonon mode energies are compared in table 2, and again the agreement is quite good.

As we can see from figure 4, half of the B_{2u} modes induce relatively small dipole moments. This is due to the fact that, for these phonons, atoms mainly oscillate along the **c** axis and the b component of the polarization is only a second-order effect [13]. However for the other half (which were labeled in figure 4), the motion is mainly along the **b** axis and therefore the induced dipole moment is significant. Animations of these modes and more information can be obtained at [26]. Figure 5 shows the most important B_{2u} modes which induce large dipole moment along the b axis. In particular, we note that the b_9 mode around 80 meV induces a significantly large dipole moment and probably it is the mode which is most responsible for the observed spontaneous polarization in NVO. This mode (i.e. b_9) is a very simple mode where the O(2) oxygens oscillate along the V–O bond as shown in figure 5. The other two high-energy modes, b_{10} and b_{11}, are very similar to the b_9 mode. In the b_{10} mode, O(1) atoms oscillate along the V–O bond and at the same time there is O–Ni(c)–O bond bending as shown in figure 5. In the highest-energy mode, b_{11}, in addition to the

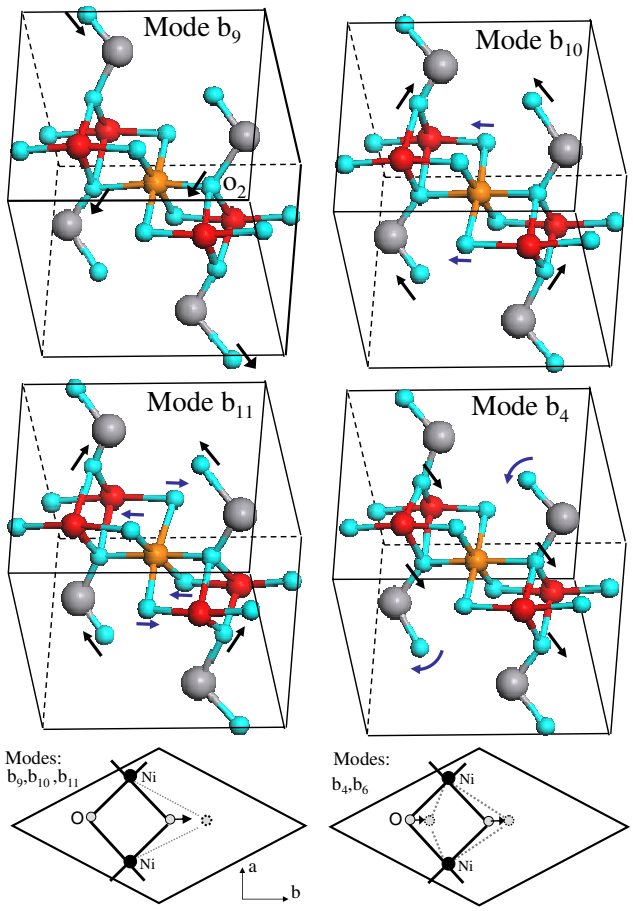

Figure 5. Some of the B_{2u} phonon modes which induce large dipole moment along the b axis. The last two panels show schematically the effect of the modes on the Ni–O–Ni bond angle.

main V–O bond stretching, we now have two O–Ni–O bond bending and therefore the mode energy is much higher. In summary, the common factor in modes, b_9, b_{10} and b_{11} is that one of the two oxygens along the Ni-spine chain oscillates along the V–O bonds. This seems to be the key mode that induces very large dipole moment along the b axis. Finally, the modes b_4 and b_6 induce dipole moments which are about $1/16$ of the dipole induced by the mode b_9. One of these two modes is shown in figure 5 where both of the oxygens which make the Ni-spine chain oscillate along the Ni–O bond. The last two panels in figure 5 show schematically how the Ni–O–Ni bond angles are affected by the b_9, b_{10}, b_{11} and b_4, b_6 modes, respectively. For modes b_9, b_{10} and b_{11}, we note that only one of the Ni–O–Ni bond angles (near 90°) changes and therefore one expects that these modes will have a significant effect on the superexchange path that is mediated through the Ni–O–Ni path. However, for modes b_4 and b_6, we note that one of the Ni–O–Ni bond angles increases while the other Ni–O–Ni bond angle decreases and therefore at first order we do not expect that these modes can have a significant effect on the exchange parameters.

In conclusion, we have identified one major mode, i.e. b_9, which induces the largest dipole moment along the b axis. It also has a direct effect on the Ni–O–Ni bond angle (only one of them) along the Ni-spine chain and therefore it is expected to couple with the magnetic interactions between Ni-spine spins.

Finally, we discuss what kind of distortion is needed in order to induce the experimentally observed spontaneous polarization whose magnitude is about $P_{\rm exp} = 1.25 \times 10^{-4}$ C m^{-2}. We note that this induced polarization is much smaller than the calculated rms dipole moment ($P_{\rm rms} \sim 176.0 \times 10^{-4}$ C m^{-2}) assuming the polarization is induced by the b_9 mode. This suggests that the local distortion should be of the order of $Q_{\rm distortion} = \frac{P_{\rm exp}}{P_{\rm rms}} Q_{\rm rms} = \frac{1.25}{176.0} \frac{1.44}{\sqrt{83.82}} \approx 0.001$ Å. This is quite a small distortion and would be very difficult to observe directly by neutron powder diffraction. However, variable temperature infrared measurements may have the needed sensitivity to probe local structural changes in the HTI, LTI and C phases of NVO.

4. Magnetic interactions

We now discuss our first-principles calculations of the superexchange interactions present in NVO. Experimentally we have two strong constraints on the exchange interactions in NVO. The first one is the ratio between NN and SNN interactions along the Ni-spine chain. This ratio, i.e. J_{1a}/J_{2a}, should be around 2.6, a value required to obtain the successive magnetic phase transitions with incommensurate structure observed in NVO. The second constraint is the Curie–Weiss constant, which is 18.7 K. As we will see below, the computed superexchange constants satisfy this constraint only if we have on-site U at an oxygen site. Having Ni(U) also gives results that are somewhat consistent with these two constraints but then the electronic bandgap in the DOS is too large.

We developed a systematic approach where the exchange parameter between spin-i and spin-j is obtained from the total energies of a reference magnetic configuration and those configurations obtained by flipping the spins i and j one at a time and simultaneous flipping of both spins. From these four energies, it is possible to obtain the exchange constant between spin i and j. We note that here we are interested in the isotropic exchange interactions. We also do not consider spin–orbit interactions in our calculations. Hence all calculations are done for collinear spin configurations.

In order to extract superexchange interactions up to a large cutoff distance, we calculated the total energy for various periodic spin configurations based on an arbitrary alignment of the z components of spin ($S_z = \pm 1$) with a $2 \times 1 \times 1$ supercell of the conventional cell of NVO which contains 112 atoms. Since the spin configuration is the same from one supercell to the next one we may write the total energy E_1 as

$$E_1 = E_0 + \tfrac{1}{2} \sum_{\mathbf{R}} \sum_{k,l} J(0,k;\mathbf{R},l) S_k(0) S_l(\mathbf{R})$$
$$= E_0 + \tfrac{1}{2} \sum_{k,l} K(k,l) S_k S_l, \qquad (4)$$

where $S(n,\mathbf{R}) \equiv S_n$ is the spin of the nth ion in the supercell at $\mathbf{R}$ and because of periodicity $K(k,l) = K(l,k) \equiv \sum_{\mathbf{R}} J(k,0;l,\mathbf{R})$. It is obvious that we can only expect to determine $K(k,l)$ and not the individual J's. However, since the supercell is reasonably large, we can identify the K's with

Table 3. The calculated magnetic interactions for all Ni pairs up to a cutoff distance of 6.5 Å as a function of U and J used in LDA + U. The last row shows the Curie–Weiss constant, which was experimentally determined to be 18.7 K [1, 4]. The ratio J_{1a}/J_{2a} for each case is shown on the third row. The experimental value for J_{1a}/J_{2a} is 2.6 [2, 4]. The spin labels are shown in figure 1. The last column (U(Ni) = 1.5 eV, J(Ni) = 1 eV and U(O) = 4.0 eV) gives the best agreement with the experimental data.

J (meV)	Dist. (Å)	$U=0$ $J=0$	$U=1.5$ $J=1$	$U=5$ $J=0$	$U=5$ $J=1$	$U=6$ $J=1$	$U=7$ $J=1$	$U=8$ $J=1$	U(O) = 4 J(O) = 0	U(O) = 4 Ni: 1, 1.5[a]
J_{1a} (s1s2)	2.961	5.73	3.53	1.24	1.16	0.85	0.62	0.45	2.96	1.71
J_{2a} (s1s3)	5.922	1.44	0.93	0.37	0.37	0.28	0.21	0.15	1.19	0.76
J_{1a}/J_{2a}		3.98	3.81	3.32	3.15	3.05	2.99	3.03	2.48	2.25
J (s1s5)	4.938	−2.24	−1.13	−0.50	−0.43	−0.33	−0.25	−0.19	−2.36	−1.17
J (s5s9)	5.062	1.86	1.25	0.47	0.50	0.38	0.30	0.22	1.5	1.02
J (s5s10)	5.865	0.68	0.37	0.09	0.10	0.07	0.05	0.03	0.55	0.30
J (s1s10)	6.411	−0.22	−0.11	−0.05	−0.05	−0.04	−0.03	−0.03	−0.20	−0.09
J (s1s6)	5.758	−0.09	0.03	−0.01	−0.01	−0.02	−0.02	−0.02	0.06	0.02
J (s1s9)	5.686	−0.08	−0.03	−0.01	−0.02	−0.01	−0.01	−0.01	−0.08	−0.02
J (s1c1)	2.932	3.45	1.59	0.52	0.38	0.27	0.20	0.14	1.34	0.28
J (s1c5)	4.914	−1.78	−0.78	−0.36	−0.28	−0.22	−0.17	−0.13	−1.92	−0.85
J (s2c1)	5.112	0.13	0.19	0.01	0.05	0.03	0.02	0.01	−0.11	0.07
J (c1c3)	5.068	−0.25	0.05	0.03	0.05	0.04	0.03	0.03	−0.43	−0.05
J (c1c2)	5.922	0.24	0.13	−0.04	−0.01	−0.03	−0.03	−0.02	0.26	0.16
J (c1c5)	6.411	0.02	0.02	0.01	0.01	0.01	0.00	0.00	0.00	0.01
Curie–Weiss Θ (K)		116.4	74.6	20.7	20.3	14.1	7.9	6.3	24.3	18.5

[a] U(Ni) = 1.5 eV and J(Ni) = 1 eV.

the J at the minimal separation. It is also obvious that we can only hope to determine $K(i, j)$ for $i \neq j$, since the energy involving $K(i, i)$ depends on $(S_i)^2 = 1$ since $S_i = \pm 1$ for Ni spins. To determine $K(i, j)$ for $i \neq j$ we calculate four total energies, E_1 and the other three corresponding energies, when we independently change the sign of S_i and S_j. When we change the sign of S_i we get

$$E_2 = E_0 + \tfrac{1}{2}\sum_{k,l} K(k,l)S_k[1-2\delta_{i,k}]S_l[1-2\delta_{i,l}], \qquad (5)$$

where $\delta_{n,m} = 1$ if $n = m$ and is zero otherwise. Likewise when we change the sign of S_j we get

$$E_3 = E_0 + \tfrac{1}{2}\sum_{k,l} K(k,l)S_k[1-2\delta_{j,k}]S_l[1-2\delta_{j,l}], \qquad (6)$$

and when we change the sign of both spins i and j we get

$$E_4 = E_0 + \tfrac{1}{2}\sum_{k,l} K(k,l)S_k[1-2\delta_{i,k}][1-2\delta_{j,k}]S_l \times [1-2\delta_{i,l}][1-2\delta_{j,l}]. \qquad (7)$$

Then we construct the quantity $X = E_1 - E_2 - E_3 + E_4$ to get

$$X = \tfrac{1}{2}\sum_{k,l} K(k,l)S_kS_l[2\delta_{i,k} + 2\delta_{i,l} - 4\delta_{i,k}\delta_{i,l}] \times [2\delta_{j,k} + 2\delta_{j,l} - 4\delta_{j,k}\delta_{j,l}]. \qquad (8)$$

Since we require that $i \neq j$, this gives

$$X = 4\,K(i,j)S_iS_j, \qquad (9)$$

from which we can extract the value of $K(i, j)$. If the supercell is large enough, one can keep only the interactions between the nearest-neighboring supercell images of the spins and therefore the calculated exchange parameter can be attributed to spin interaction between the closest pairs of spins of types i and j. We also note that there are cases where spin j is at the midpoint between spin $S_i(0)$ and one of its images at $S_i(\mathbf{R})$. In that case, the calculated superexchange constant is twice J_{ij}. Similarly there are cases where the spin j is at a point where it interacts equally with four images of the spin i. In those cases, the calculated J is four times J_{ij}.

Table 3 summarizes our results for all possible exchange constants up to a cutoff distance of 6.5 Å for different on-site Coulomb repulsion U and Coulomb exchange J (which should not be confused with the superexchange constants). Usually the net effect in LDA + U is to replace U by $(U - J)$. We note that, for U(Ni) = 0, the superexchange parameters are too large (see the Curie–Weiss constant). Also the ratio J_{1a}/J_{2a} is too large (i.e. for U(Ni) = 0, the ratio is 3.98, but experimentally is 2.6). Increasing U(Ni) improves the J's. The ratio goes down to 3.0 and saturates there. From the Curie–Weiss constant, the best solution seems to be around U(Ni) = 5.0 eV and J(Ni) = 1.0 eV. These numbers are typical for Ni-based oxide materials. However, the problem is that we have too large an electronic bandgap with U(Ni) = 5 eV, which is inconsistent with the experiment. On the other hand, including U at the oxygen site improves the results significantly. As we discussed above, U(O) does not affect the phonon spectrum which agrees well with the experimental data. U(O) also does not open a gap. Hence, basically using U(O) of the order of 4.0 eV, we can get exchange parameters that are consistent with experiment and at the same time we still have a good phonon spectrum and correct bandgap. Interestingly, with U(O), it is very easy to get the correct value for the ratio J_{1a}/J_{2a}, which was not the case without U(O). In table 3, we also present a solution where we have both U(Ni) and U(O) which seems to give the best agreement with the experiment.

From table 3, it is clear that the energy scale of the superexchange interactions depends strongly on the value assigned to U. However, a nice result is apparent: the

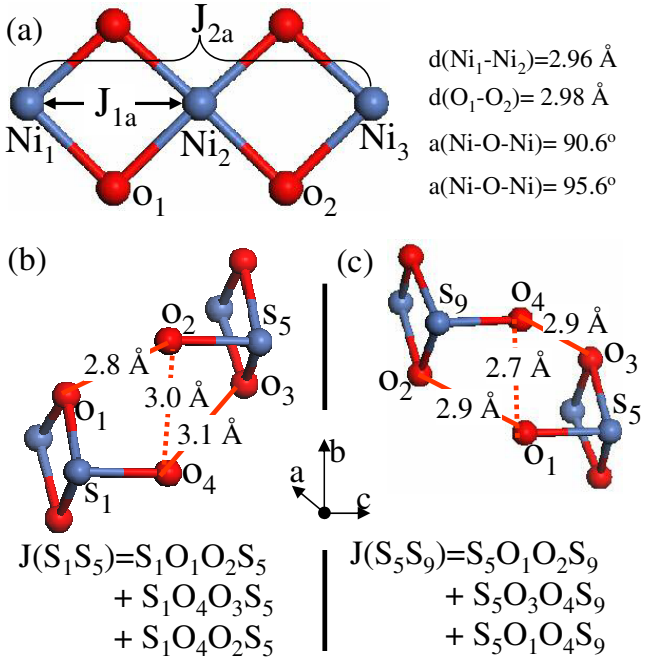

Figure 6. The most important (i.e. the largest) superexchange interactions between Ni ions according to LDA + U calculations listed in table 3.

ordering (from largest magnitude to smallest magnitude) of the exchange interactions is independent of the choice of U. Another nice result concerns how the exchange interactions are consistent with the observed magnetic structure. The magnetic structure of both the commensurate and incommensurate phases [4] is such that the spins along the **b** and **c** directions are antiferromagnetically arranged. In [4] a tentative assignment of values for the exchange integrals was given, assuming that this antiferromagnetic arrangement was caused by NN antiferromagnetic interactions along the **b** and **c** directions. With this assumption, the correct value of the Curie–Weiss constant Θ could only be obtained using rather small values of the exchange interactions in the **b** and **c** directions. The calculations of the present paper resolve such difficulties: the antiferromagnetic arrangement along the **b** axis is not generated by an antiferromagnetic interaction between spins s1 and s9 (this interaction is very weak), but is rather due to a much stronger *ferromagnetic* interaction between spins s1 and s5 which, in combination with the s5–s9 antiferromagnetic interaction, has the effect of forcing spins s1 and s9 to be anti-parallel. Since the contribution to Θ depends on the algebraic sum of the exchange interactions, the fact that one of the dominant interactions is ferromagnetic is consistent with larger (and more satisfactory) values of the other exchange interactions.

Figure 6 shows some of the J values that we determined as the major superexchange interactions. In addition to the major J_{1a} and J_{2a} interactions along the spine chain, surprisingly we find that there are strong interactions between s1–s5 (see figure 1 for spin numbering) and s1–s9. Note that the s1–s5 interaction is between two adjacent Kagomé planes while s1–s9 is within the same Kagomé plane.

After having determined the most important superexchange interactions, the next step is to find out how they couple with the B_{2u} phonons, in particular the b_9 mode that we discussed above. Currently we are calculating the phonon derivatives of the superexchange interactions listed in table 3 from which we hope to identify the spin–phonon coupling. By plotting $\mathrm{d}J/\mathrm{d}Q_n$, where Q_n is the amplitude of the nth zero wavevector phonon mode, we should be able to extract both linear and quadratic coupling. Needless to say, these sorts of calculations are computationally very expensive and will be published elsewhere. In this review, instead of giving actual phonon derivatives of J, in the next section, we will discuss qualitatively how spin–phonon coupling takes place in multiferroics via coupling which involves two spin operators (to preserve time reversal symmetry) and either one (QSS) or two phonons (QQSS) as written in equations (12), (14) and (15).

5. Magnon–phonon interaction

Here we make some qualitative remarks about the spin–phonon interaction in multiferroics, which we write as $V_{\mathrm{sp}} \equiv V^{(3)} + V^{(4)}$, where

$$V^{(3)} = \sum_{\mathbf{r}\mathbf{r}'} \sum_{\alpha\beta\gamma} M^{(1)}_{\alpha\beta\gamma}(\mathbf{r},\mathbf{r}') S_\alpha(\mathbf{r}) S_\beta(\mathbf{r}') \times [u_\gamma(\mathbf{r}) - u_\gamma(\mathbf{r}')] \tag{10}$$

and

$$V^{(4)} = \sum_{\mathbf{r}\mathbf{r}'} \sum_{\alpha\beta\gamma\delta} M^{(2)}_{\alpha\beta\gamma\delta}(\mathbf{r},\mathbf{r}') S_\alpha(\mathbf{r}) S_\beta(\mathbf{r}') \times [u_\gamma(\mathbf{r}) - u_\gamma(\mathbf{r}')][u_\delta(\mathbf{r}) - u_\delta(\mathbf{r}')], \tag{11}$$

where $M^{(n)}$ is the nth gradient of the exchange tensor with respect to ionic displacements and $u_\gamma(\mathbf{r})$ is the γ component of the displacement of the ion from its equilibrium position at $\mathbf{r}$. All displacements are taken relative to the paraelectric and paramagnetic phase. To see the effect of these terms we construct an effective quadratic Hamiltonian obtained using a Hartree decoupling of the above interactions, which involves replacing operators or products of operators by their thermal expectation values indicated by $\langle\cdots\rangle$. In so doing we note that $\langle u_\alpha(\mathbf{r})\rangle$ is very small—in fact, so small that in NVO no direct observation of this quantity has been made, even though its non-zero value is guaranteed by the existence of a spontaneous polarization. Accordingly, we replace $V^{(3)}$ by

$$V^{(3)}_{\mathrm{eff}} = \sum_{\mathbf{r}\mathbf{r}'} \sum_{\beta\gamma} N_{\beta\gamma}(\mathbf{r},\mathbf{r}') S_\beta(\mathbf{r}')[u_\gamma(\mathbf{r}) - u_\gamma(\mathbf{r}')], \tag{12}$$

where

$$N_{\beta\gamma}(\mathbf{r},\mathbf{r}') = \sum_\alpha [M^{(1)}_{\alpha\beta\gamma}(\mathbf{r},\mathbf{r}')\langle S_\alpha(\mathbf{r})\rangle + M^{(1)}_{\beta\alpha\gamma}(\mathbf{r}',\mathbf{r})\langle S_\alpha(\mathbf{r}')\rangle]. \tag{13}$$

The effect of $V^{(3)}_{\mathrm{eff}}$ is [27–31] to (a) shift the spectral weight from optical phonons into low frequency magnons and (b) concomitantly shift the energies of these two coupled excitations. The shift in spectral weight is such that the change in the IR absorption cross section due to $V^{(3)}_{\mathrm{eff}}$ is of the order $I_0[V^{(3)}_{\mathrm{eff}}/\omega_{\mathrm{p}}]^2 \sim I_0[N^2/(m\omega^3_{\mathrm{p}})]$, where m is an ionic mass,

ω_p is a phonon energy (assumed to be large compared to the magnon energy) and I_0 is the IR absorption cross section in the absence of $V_{\rm eff}^{(3)}$. The magnitude of the energy shift (upward for the phonon and downward for the magnon) is of the order $N^2/(m\omega_p^2)$. Thus, as the coupling is seen to increase with decreasing temperature, the energy shifts should also increase. For $Eu_{0.75}Y_{0.25}MnO_3$ [29] the relationship between the energy shifts and the transfer of spectral weight (as measured by the optical absorption or the effect on the static dielectric constant) is not seen: the observed 5 cm^{-1} optical phonon frequency shift is not consistent with the 20 cm^{-1} predicted by the model of [28] when scaled to explain the decrease in spectral weight as it should if only $V^{(3)}$ were operative [29]. One is therefore led to consider the effects of $V^{(4)}$, again within a Hartree decoupling scheme. The term

$$V_{\rm eff}^{(4,a)} = \sum_{\mathbf{rr'}} \sum_{\alpha\beta\gamma\delta} M^{(2)}_{\alpha\beta\gamma\delta}(\mathbf{r},\mathbf{r'}) S_\alpha(\mathbf{r}) S_\beta(\mathbf{r'}) \times \langle [u_\gamma(\mathbf{r}) - u_\gamma(\mathbf{r'})][u_\delta(\mathbf{r}) - u_\delta(\mathbf{r'})]\rangle \quad (14)$$

will induce a very slight temperature dependence into the exchange coupling. The term

$$V_{\rm eff}^{(4,b)} = \sum_{\mathbf{rr'}} \sum_{\alpha\beta\gamma\delta} M^{(2)}_{\alpha\beta\gamma\delta}(\mathbf{r},\mathbf{r'}) \langle S_\alpha(\mathbf{r}) S_\beta(\mathbf{r'})\rangle \times [u_\gamma(\mathbf{r}) - u_\gamma(\mathbf{r'})][u_\delta(\mathbf{r}) - u_\delta(\mathbf{r'})] \quad (15)$$

is more important, as discussed in [32], because this term induces a dependence of the phonon dynamical matrix on the spin ordering, which gives rise to an observable temperature dependence of the optical phonon frequencies. Note that this term does not produce a linear spin–phonon coupling (we assume $\langle u\rangle$ to be zero), and hence it does not shift the spectral weight. But it does shift the energies by an amount of the order

$$\frac{M^{(2)}\langle S\rangle^2}{m\omega_p}, \quad (16)$$

where ω_p is the phonon energy in the absence of spin–phonon coupling. Note that, although this term is proportional to the second gradient of the exchange tensor, it leads to an energy shift at first order in perturbation theory, whereas the effect of $V_{\rm eff}^{(3)}$ only appears at second-order perturbation theory. In fact, the ratio of the quartic energy to the cubic energy is of the order $\omega_p[\partial^2 J/\partial u^2]/[\partial J/\partial u]^2$. There is an ancient empirical rule of thumb that J is proportional to r^{-10} [33], which would give this ratio to be ω_p/J, which is of the order of 10. Accordingly, it is suggested [34] that this energy shift can easily account for the 15 cm^{-1} discrepancy mentioned above for the optical phonon in $Eu_{0.75}Y_{0.25}MnO_3$ [29].

6. Conclusions

In this review we have presented a detailed study of the zone-center phonons and the superexchange integrals calculated within the LDA + U approach. The aim of our study is to determine which of the zone-center phonons are relevant and which superexchange parameters are important for the observed magnetic structure and spontaneous polarization in NVO. This work will therefore set the stage for a separate quantum calculation of the derivatives of the exchange tensor with respect to atomic displacements.

We compared our calculations with available inelastic neutron and polarized IR measurements and obtained excellent agreement for both the energies and the intensities. We identified one particular mode near 80 meV which induces significant dipole moment along the b axis. This mode also has a direct effect on the Ni–O–Ni bond angle and therefore is expected to couple strongly with the magnetic interactions. Using the calculated Born-effective charges and the eigenvectors we conclude that the required distortion to induce the observed dipole moment is small (0.001 Å) and would be difficult to observe directly by neutron powder diffraction.

This work, summarizing vibrational mode assignments, their symmetries and the predicted contribution of b-polarized displacements to the spontaneous polarization, will surely stimulate efforts to explore magnetic ordering-induced lattice distortions in $Ni_3V_3O_8$, as well as in the quasi-isostructural Co and Mn analogs.

Acknowledgments

Work at the University of Tennessee is supported by the Materials Science Division, Basic Energy Sciences, US Department of Energy (DE-FG02-01ER45885). JI thanks support from the Spanish (FIS2006-12117-C04-01) and Catalan (SGR2005-683) governments.

References

[1] Rogado N, Lawes G, Huse D A, Ramirez A P and Cava R J 2002 *Solid State Commun.* **124** 229
[2] Lawes G, Kenzelmann M, Rogado N, Kim K H, Jorge G A, Cava R J, Aharony A, Entin-Wohlman O, Harris A B, Yildirim T, Huang Q A, Park S, Broholm C and Ramirez A P 2004 *Phys. Rev. Lett.* **93** 247201
[3] Lawes G, Harris A B, Kimura T, Rogado N, Cava R J, Aharony A, Entin-Wohlman O, Yildirim T, Kenzelmann M, Broholm C and Ramirez A P 2005 *Phys. Rev. Lett.* **95** 087205
[4] Kenzelmann M, Harris A B, Aharony A, Entin-Wohlman O, Yildirim T, Huang Q, Park S, Lawes G, Broholm C, Rogado N, Cava R J, Kim K H, Jorge G and Ramirez A P 2006 *Phys. Rev.* B **74** 014429
[5] Hur N, Park S, Sharma P A, Ahn J S, Guha S and Cheong S-W 2004 *Nature* **429** 392
[6] Kenzelmann M, Harris A B, Jonas S, Broholm C, Schefer J, Kim S B, Zhang C L, Cheong S-W, Vajk O P and Lynn J W 2005 *Phys. Rev. Lett.* **95** 087206
[7] Harris A B and Lawes G 2007 Ferroelectricity in incommensurate magnets *The Handbook of Magnetism and Advanced Magnetic Materials* ed H Kronmuller and S Parkin (Chichester: Wiley) pp 2428–60
[8] Sauerbrei E E, Faggiani F and Calvo C 1973 *Acta Crystallogr.* B **29** 2304
[9] Wilson A J C 1995 *International Tables for Crystallography* vol A (Dordrecht: Kluwer–Academic)
[10] Tornow S, Entin-Wohlman O and Aharony A 1999 *Phys. Rev.* B **60** 10206
[11] Kaplan T A 1961 *Phys. Rev.* **124** 329
[12] Nagamiya T 1967 *Solid State Physics* vol 29, ed F Seitz and D Turnbull (New York: Academic) p 346

[13] Harris A B, Yildirim T, Aharony A and Entin-Wohlman O 2006 *Phys. Rev.* B **73** 184433
[14] Rai R C, Cao J, Vergara L I, Brown S, Musfeldt J L, Singh D J, Lawes G, Rogado N, Cava R J and Wei X 2007 *Phys. Rev.* B **76** 174414
[15] Rai R C, Cao J, Brown S, Musfeldt J L, Kasinathan D, Singh D J, Lawes G, Rogado N, Cava R J and Wei X 2006 *Phys. Rev.* B **74** 235101
[16] Perdew J P, Burke K and Ernzerhof M 1996 *Phys. Rev. Lett.* **77** 3865
[17] Hohenberg P C and Kohn W 1964 *Phys. Rev.* **136** B864
Kohn W and Sham L J 1965 *Phys. Rev.* **140** A1133
[18] Kresse G and Furthmüller J 1996 *Comput. Mater. Sci.* **6** 15
[19] Blöchl P E 1994 *Phys. Rev.* B **50** 17953
[20] Anisimov V I, Aryasetiawan F and Lichtenstein A I 1997 *J. Phys.: Condens. Matter* **9** 767
[21] Nekrasov I A, Korotin M A and Anisimov V I 2000 *Preprint* cond-mat/0009107
[22] Yildirim T 2000 *Chem. Phys.* **261** 205
[23] Copley J R D, Neumann D A and Kamitakahara W A 1995 *Can. J. Phys.* **73** 763
[24] Bernardini F, Fiorentini V and Vanderbilt D 1997 *Phys. Rev.* B **56** R10024
[25] Wooten F 1972 *Optical Properties of Solids* (New York: Academic)
[26] Animations of the B_{2u} phonons can be found at http://www.ncnr.nist.gov/staff/taner/nvo
[27] Pimenov A, Mukhin A A, Ivanov V Yu, Travkin V D, Balbashov A M and Loidl A 2006 *Nat. Phys.* **2** 97
[28] Katsura H, Balatsky A V and Nagaosa N 2007 *Phys. Rev. Lett.* **98** 027203
[29] Valdés Aguilar R, Sushkov A M, Zhang C L, Choi Y-J, Cheong S-W and Drew H D 2007 *Phys. Rev.* B **76** 060404
[30] Pimenov A, Rudolf T, Mayr F, Loidl A, Mukhin A A and Balbashov A M 2006 *Phys. Rev.* B **74** 100403(R)
[31] Sushkov A B, Valdés Aguillar R V, Park S, Cheong S-W and Drew H D 2007 *Phys. Rev. Lett.* **98** 027202
[32] Fennie C J and Rabe K 2006 *Phys. Rev. Lett.* **96** 205505
[33] Bloch D 1966 *J. Phys. Chem. Solids* **27** 881
[34] Harris A B 2007 *Phys. Rev.* B **76** 054447